Computers and Structures 182 (2017) 404–418

Contents lists available at ScienceDirect

Computers and Structures

journal homepage: www.elsevier.com/locate/compstruc

A new MITC4+ shell element

Yeongbin Ko [a], Phill-Seung Lee [a,*], Klaus-Jürgen Bathe [b]

[a] Department of Mechanical Engineering, Korea Advanced Institute of Science and Technology, 291 Daehak-ro, Yuseong-gu, Daejeon 34141, Republic of Korea
[b] Department of Mechanical Engineering, Massachusetts Institute of Technology, Cambridge, MA 02139, USA

ARTICLE INFO

Article history:
Received 21 September 2016
Accepted 9 November 2016
Available online 18 January 2017

Keywords:
Shell structures
Shell finite elements
4-node element
MITC method
MITC4 element
Shear and membrane locking

ABSTRACT

We presented in Ko et al. (2016) an MITC4+ shell element that shows a much improved convergence behavior when compared to the widely used MITC4 (Dvorkin and Bathe, 1984) shell element. However, the element does still not show optimal convergence behavior when used in distorted meshes in the analysis of some shell problems. In the present paper, we establish a new MITC4+ shell element which shows significantly improved and indeed an almost optimal convergence behavior. In this new continuum mechanics-based shell element, the shear locking is alleviated using the well-known assumed transverse shear strain field of the original MITC4 shell element and the membrane locking is alleviated using a new assumed membrane strain field. The new MITC4+ shell element passes all basic tests: the isotropy, zero energy mode and patch tests. The excellent performance of the shell element is demonstrated through convergence studies in the solution of well-selected behavior-encompassing shell benchmark problems.

1. Introduction

In the finite element analysis of shell structures, the development of "ideal" shell finite elements that satisfy the ellipticity, consistency and inf-sup conditions have been pursued with high interest [3–6]. Such shell elements should not contain an adjustable numerical factor, pass the basic tests (the isotropy, zero energy mode and patch tests) as well as show uniformly optimal convergence behavior for any shell problem solved with uniform (regular) or distorted meshes regardless of the asymptotic category of the problem (with membrane-dominated, bending-dominated, or mixed shell behavior). Of course, the category of a shell problem depends on the shell geometry, loading and boundary conditions [6–8].

The major obstacles in the development of shell finite elements are shear and membrane locking. To alleviate the locking behaviors, the MITC (Mixed Interpolation of Tensorial Components) method was established to obtain various quadrilateral and triangular shell finite elements [1–3,9–18]. Of particular interest are 4-node continuum mechanics based elements, and here the convergence behavior of the 4-node MITC element (MITC4) [2] is observed to be close to uniformly optimal in the solution of many problems when uniform meshes are used due to the effective treatment of shear locking. The MITC4 shell element is widely used in engineering practice, but since membrane locking is not treated in the element formulation, the solution accuracy can deteriorate when curved geometries are solved with distorted meshes [1,19].

In Ref. [1], we presented an improved MITC4 shell element, named the MITC4+ element, which showed better convergence behavior, however not an optimal or ideal behavior when distorted meshes are used in the solution of doubly-curved shells.

There have been several attempts to alleviate the membrane locking of 4-node continuum mechanics based shell finite elements. The method of reduced integration [20–22] can greatly alleviate membrane locking as well as shear locking, but the elements suffer from rank deficiency and do not properly represent physical rigid body modes, needing undesirable stabilization and displacement projection techniques. The method of assumed strains [1,12,23–25] was applied to the membrane strains (in-plane strains evaluated at the mid-surface) to alleviate membrane locking.

In these developments, the assumed membrane strain field proposed by Choi and Paik is very interesting [23]. The field greatly eliminates membrane locking of 4-node continuum mechanics based shell elements, but the element fails the membrane patch test. In a subsequent development, Cho and Roh successfully applied the assumed membrane strain field and developed a 4-node exact geometry shell element [24], and Kulikov and Plotnikova developed a methodology to overcome locking in a

* Corresponding author.
E-mail address: phillseung@kaist.edu (P.S. Lee).

http://dx.doi.org/10.1016/j.compstruc.2016.11.004
0045-7949/

4-node exact geometry shell element [25]. Geometry exact shell elements are formulated using mathematical shell models with the exact representation of shell mid-surfaces [6,7,24–26], and thus membrane locking can be investigated with relative ease. However, in continuum mechanics based shell finite elements, curvatures do not explicitly appear in the element formulations, which makes it difficult to identify how to alleviate locking and thus formulate a generally applicable element for any shell geometry and boundary conditions.

Our objective in this paper is to give an effective 4-node continuum mechanics based shell element, in which shear and membrane locking are greatly reduced by employing the MITC method. The shear locking is resolved using the well-known assumed transverse shear strain field of the original MITC4 shell element [2], and we focus on the development of a new assumed membrane strain field to alleviate membrane locking. Doing so, we first extract the membrane strains in the shell element formulation with the strains represented in terms of characteristic geometry and displacement vectors. We then start with the membrane strain field proposed by Choi and Paik [23], adopt the idea of Kulikov and Plotnikova [25], and reach the new element formulation to also alleviate membrane locking. The resulting shell element, the new MITC4+ element, passes all basic tests and shows excellent convergence behavior in the analysis of various difficult well-chosen shell problems even when using distorted meshes. The element shows a significantly better convergence behavior than the MITC4+ shell element previously published [1].

In the following sections, the formulation of the MITC4 shell element is briefly reviewed and then the formulation of the new MITC4+ shell element is presented. The performance of the new shell element is illustrated through the basic tests as well as the established convergence tests.

2. The MITC4 shell finite element

In this section, we briefly review the formulation of the MITC4 shell element.

The geometry of a standard 4-node continuum mechanics based quadrilateral shell finite element is interpolated using [1–3]

$$\mathbf{x}(r,s,t)=\sum_{i=1}^{4}h_i(r,s)\mathbf{x}_i+\frac{t}{2}\sum_{i=1}^{4}a_i h_i(r,s)\mathbf{V}_n^i, \tag{1}$$

where $h_i(r,s)$ is the two-dimensional interpolation function of the standard isoparametric procedure corresponding to node i, $\mathbf{x}_i$ is the position vector of node i in the global Cartesian coordinate system, and a_i and $\mathbf{V}_n^i$ denote the shell thickness and the director vector at the node, respectively, see Fig. 1.

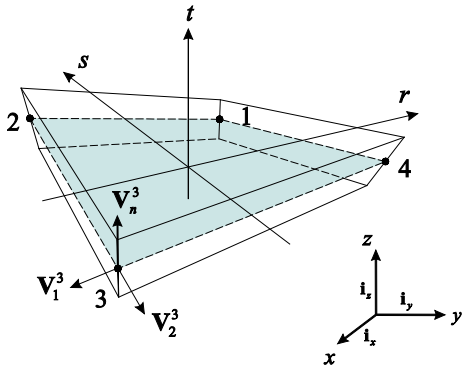

Fig. 1. A standard 4-node quadrilateral continuum mechanics based shell finite element.

It is useful to note the following representation of interpolation function $h_i(r,s)$:

$$\begin{aligned} &h_i(r,s)=\frac{1}{4}(1+\xi_i r)(1+\eta_i s) \quad \text{with} \quad i=1,2,3,4,\\ &[\,\xi_1 \quad \xi_2 \quad \xi_3 \quad \xi_4\,]=[\,1 \quad -1 \quad -1 \quad 1\,],\\ &[\,\eta_1 \quad \eta_2 \quad \eta_3 \quad \eta_4\,]=[\,1 \quad 1 \quad -1 \quad -1\,], \end{aligned} \tag{2}$$

in which ξ_i and η_i are permuted together.

The corresponding displacement interpolation of the element is

$$\mathbf{u}(r,s,t)=\sum_{i=1}^{4}h_i(r,s)\mathbf{u}_i+\frac{t}{2}\sum_{i=1}^{4}a_i h_i(r,s)(-\mathbf{V}_2^i\alpha_i+\mathbf{V}_1^i\beta_i), \tag{3}$$

in which $\mathbf{u}_i$ is the nodal displacement vector in the global Cartesian coordinate system, $\mathbf{V}_1^i$ and $\mathbf{V}_2^i$ are unit vectors orthogonal to $\mathbf{V}_n^i$ and to each other, and α_i and β_i are the rotations of the director vector $\mathbf{V}_n^i$ about $\mathbf{V}_1^i$ and $\mathbf{V}_2^i$, respectively, at node i.

The linear terms of the displacement-based covariant strain components are given by

$$e_{ij}=\frac{1}{2}(\mathbf{g}_i\cdot\mathbf{u}_{,j}+\mathbf{g}_j\cdot\mathbf{u}_{,i}), \tag{4}$$

in which

$$\mathbf{g}_i=\frac{\partial\mathbf{x}}{\partial r_i}, \quad \mathbf{u}_{,i}=\frac{\partial\mathbf{u}}{\partial r_i} \quad \text{with } r_1=r, r_2=s, r_3=t. \tag{5}$$

For the MITC4 shell element, the covariant in-plane strain components are calculated using Eqs. (1)–(3) without any modification. The transverse shear strain field is based on assuming constant covariant transverse shear strain conditions along the edges, see Ref. [2]

$$\begin{aligned} \tilde{e}_{rt}&=\frac{1}{2}(1+s)e_{rt}^{(A)}+\frac{1}{2}(1-s)e_{rt}^{(B)},\\ \tilde{e}_{st}&=\frac{1}{2}(1+r)e_{st}^{(C)}+\frac{1}{2}(1-r)e_{st}^{(D)}, \end{aligned}$$

where the tying points are shown in Fig. 2 [1,9].

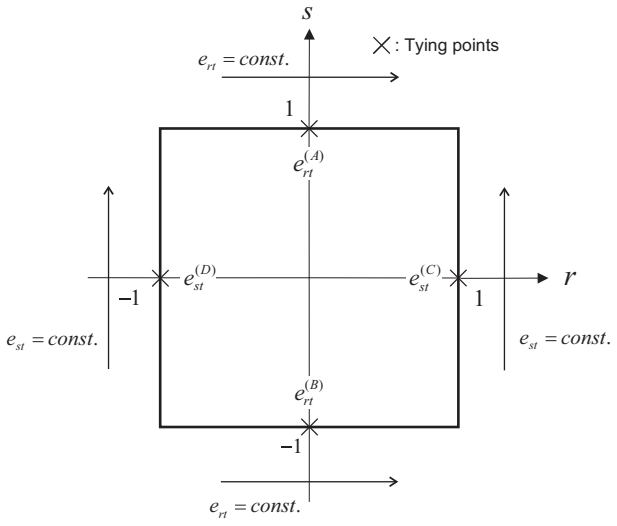

Fig. 2. Tying positions (A)–(D) for the assumed transverse shear strain field of the MITC4 shell element. The constant transverse shear strain conditions are imposed along its edges.

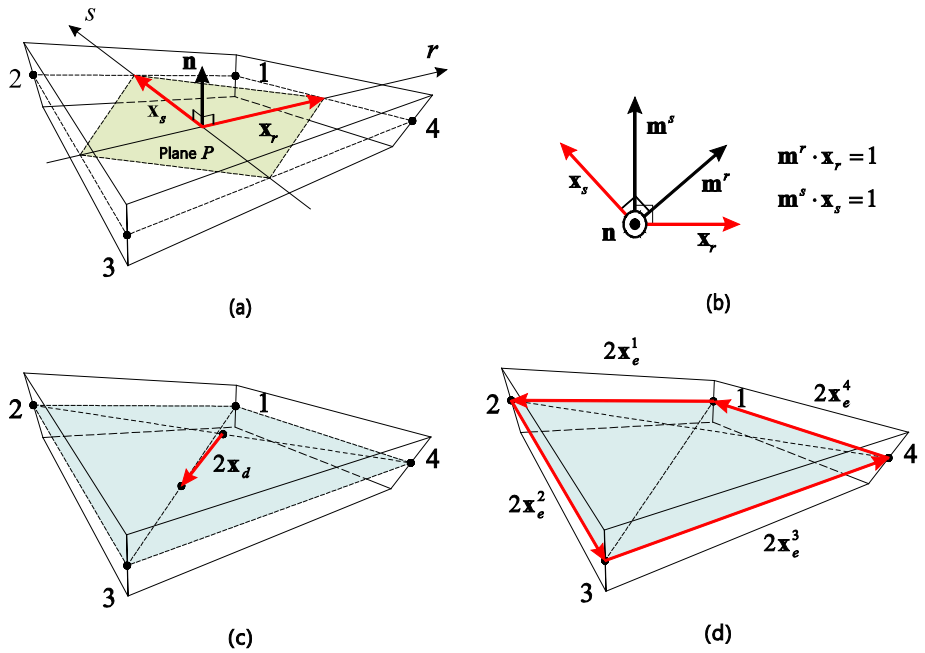

Fig. 3. Representative vectors for the element geometry. (a) Two in-plane vectors $\mathbf{x}_r$ and $\mathbf{x}_s$, and the plane P with normal vector $\mathbf{n}$. (b) Two in-plane vectors $\mathbf{m}^r$ and $\mathbf{m}^s$. (c) Distortion vector $\mathbf{x}_d$. (d) Four edge vectors $\mathbf{x}_e^1, \mathbf{x}_e^2, \mathbf{x}_e^3$ and $\mathbf{x}_e^4$.

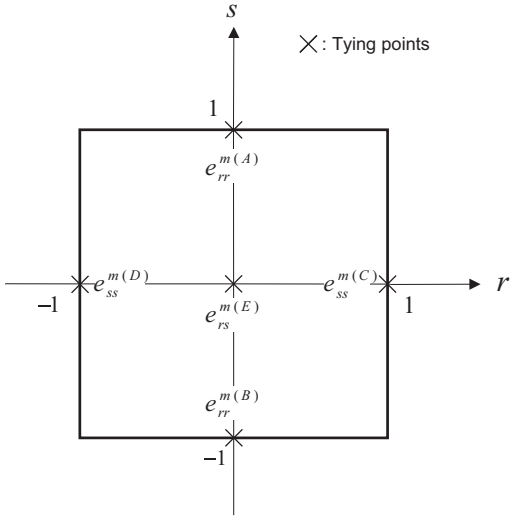

Fig. 4. Tying positions (A)–(E) for the assumed membrane shear strain field.

3. The new MITC4+ shell element

We present in this section the formulation of the new MITC4+ shell element. The covariant membrane strains are represented using characteristic geometry and displacement vectors.

3.1. Covariant membrane strains and characteristic vectors

We can write the covariant in-plane strain components in Eq. (4) as

$$e_{ij} = e_{ij}^m + t\,e_{ij}^{b1} + t^2 e_{ij}^{b2} \quad \text{with } i,j = 1,2, \tag{7a}$$

$$e_{ij}^m = \frac{1}{2}\left(\frac{\partial \mathbf{x}_m}{\partial r_i}\cdot\frac{\partial \mathbf{u}_m}{\partial r_j} + \frac{\partial \mathbf{x}_m}{\partial r_j}\cdot\frac{\partial \mathbf{u}_m}{\partial r_i}\right), \tag{7b}$$

$$e_{ij}^{b1} = \frac{1}{2}\left(\frac{\partial \mathbf{x}_m}{\partial r_i}\cdot\frac{\partial \mathbf{u}_b}{\partial r_j} + \frac{\partial \mathbf{x}_m}{\partial r_j}\cdot\frac{\partial \mathbf{u}_b}{\partial r_i} + \frac{\partial \mathbf{x}_b}{\partial r_i}\cdot\frac{\partial \mathbf{u}_m}{\partial r_j} + \frac{\partial \mathbf{x}_b}{\partial r_j}\cdot\frac{\partial \mathbf{u}_m}{\partial r_i}\right), \tag{7c}$$

$$e_{ij}^{b2} = \frac{1}{2}\left(\frac{\partial \mathbf{x}_b}{\partial r_i}\cdot\frac{\partial \mathbf{u}_b}{\partial r_j} + \frac{\partial \mathbf{x}_b}{\partial r_j}\cdot\frac{\partial \mathbf{u}_b}{\partial r_i}\right), \tag{7d}$$

with

$$\mathbf{x}_m = \sum_{i=1}^{4} h_i(r,s)\mathbf{x}_i, \quad \mathbf{x}_b = \frac{1}{2}\sum_{i=1}^{4} a_i h_i(r,s)\,\mathbf{V}_n^i, \tag{8a}$$

$$\mathbf{u}_m = \sum_{i=1}^{4} h_i(r,s)\mathbf{u}_i, \quad \mathbf{u}_b = \frac{1}{2}\sum_{i=1}^{4} a_i h_i(r,s)\,(-\mathbf{V}_2^i\alpha_i + \mathbf{V}_1^i\beta_i). \tag{8b}$$

The first term e_{ij}^m in Eq. (7a) is the covariant in-plane membrane strain at the shell mid-surface ($t = 0$), and the remaining terms are the covariant in-plane strains due to bending. The in-plane membrane strain, see Eq. (7b), can in general induce locking and it is this term that we modify as described below; we leave the other terms in Eq. (7a) as they are and evaluate them using the displacement formulation.

Using Eq. (2) in Eqs. (8a) and (8b), we obtain the following relations:

$$\frac{\partial \mathbf{x}_m}{\partial r} = \mathbf{x}_r + s\mathbf{x}_d, \quad \frac{\partial \mathbf{x}_m}{\partial s} = \mathbf{x}_s + r\mathbf{x}_d, \quad \frac{\partial \mathbf{u}_m}{\partial r} = \mathbf{u}_r + s\mathbf{u}_d, \quad \frac{\partial \mathbf{u}_m}{\partial s} = \mathbf{u}_s + r\mathbf{u}_d,$$

with

$$\begin{aligned} &\mathbf{x}_r = \frac{1}{4}\sum_{i=1}^{4}\xi_i\mathbf{x}_i, \quad \mathbf{x}_s = \frac{1}{4}\sum_{i=1}^{4}\eta_i\mathbf{x}_i, \quad \mathbf{x}_d = \frac{1}{4}\sum_{i=1}^{4}\xi_i\eta_i\mathbf{x}_i, \\ &\mathbf{u}_r = \frac{1}{4}\sum_{i=1}^{4}\xi_i\mathbf{u}_i, \quad \mathbf{u}_s = \frac{1}{4}\sum_{i=1}^{4}\eta_i\mathbf{u}_i, \quad \mathbf{u}_d = \frac{1}{4}\sum_{i=1}^{4}\xi_i\eta_i\mathbf{u}_i \end{aligned} \tag{9}$$

in which the characteristic geometry vectors $\mathbf{x}_r, \mathbf{x}_s$ and $\mathbf{x}_d$ arise naturally from the nodal point positions, see Fig. 3, and the corresponding displacement vectors are $\mathbf{u}_r, \mathbf{u}_s$ and $\mathbf{u}_d$. Note that the geometry

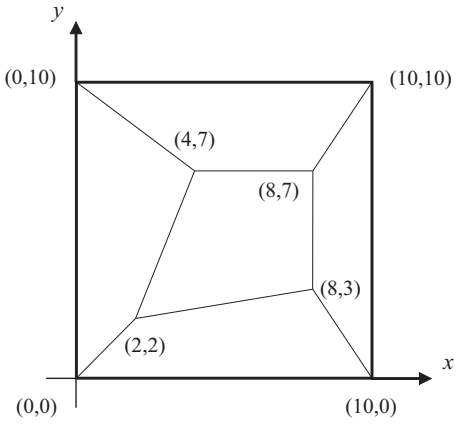

Fig. 5. Mesh geometry used for the patch tests.

vector $\mathbf{x}_d$ connects the centers of two diagonal lines in the element geometry.

The two vectors $\mathbf{x}_r$ and $\mathbf{x}_s$ form the plane P with the normal vector $\mathbf{n}$

$$\mathbf{n} = \frac{\mathbf{x}_r \times \mathbf{x}_s}{\|\mathbf{x}_r \times \mathbf{x}_s\|}, \tag{10}$$

as shown in Fig. 3(a). For an arbitrarily distorted shell element, the plane P is the only flat surface that can be defined by equally accounting for the geometry of each nodal point, as required for passing the isotropy test. Since the two in-plane vectors, $\mathbf{x}_r$ and $\mathbf{x}_s$, are not orthogonal, it is convenient to define their dual basis vectors, $\mathbf{m}^r$ and $\mathbf{m}^s$ on the plane P, such that

$$\mathbf{m}^{r_i} \cdot \mathbf{x}_{r_j} = \delta^i_j, \quad \mathbf{m}^{r_i} \cdot \mathbf{n} = 0 \quad \text{with } r_1 = r, r_2 = s, \tag{11}$$

as shown in Fig. 3(b).

Since membrane locking occurs due to out-of-plane distortions of the element geometry, the 'distortion vector' $\mathbf{x}_d$, shown in Fig. 3(c), is of particular interest. The length of the distortion vector becomes nonzero for both in-plane and out-of-plane distortions of the element geometry. The distortion vector can be decomposed into in-plane and out-of-plane components using the geometry vectors ($\mathbf{x}_r$, $\mathbf{x}_s$ and $\mathbf{n}$):

$$\mathbf{x}_d = (\mathbf{x}_d \cdot \mathbf{m}^r)\mathbf{x}_r + (\mathbf{x}_d \cdot \mathbf{m}^s)\mathbf{x}_s + (\mathbf{x}_d \cdot \mathbf{n})\mathbf{n}, \tag{12}$$

in which the dual basis vectors $\mathbf{m}^r$ and $\mathbf{m}^s$ 'measure' the distortion in the direction of in-plane vectors $\mathbf{x}_r$ and $\mathbf{x}_s$, the values $\mathbf{m}^r \cdot \mathbf{x}_d$ and $\mathbf{m}^s \cdot \mathbf{x}_d$ are the corresponding in-plane distortions, and $\mathbf{x}_d \cdot \mathbf{n}$ corresponds to the out-of-plane distortion.

In addition, the 'edge vectors' which lie along the element edges are

$$\begin{aligned}
\mathbf{x}^1_e &= \frac{\mathbf{x}_2 - \mathbf{x}_1}{2} = -\mathbf{x}_r - \mathbf{x}_d = -\frac{\partial \mathbf{x}_m}{\partial r}(0,1),\\
\mathbf{x}^2_e &= \frac{\mathbf{x}_3 - \mathbf{x}_2}{2} = -\mathbf{x}_s + \mathbf{x}_d = -\frac{\partial \mathbf{x}_m}{\partial s}(-1,0),\\
\mathbf{x}^3_e &= \frac{\mathbf{x}_4 - \mathbf{x}_3}{2} = \mathbf{x}_r - \mathbf{x}_d = \frac{\partial \mathbf{x}_m}{\partial r}(0,-1),\\
\mathbf{x}^4_e &= \frac{\mathbf{x}_1 - \mathbf{x}_4}{2} = \mathbf{x}_s + \mathbf{x}_d = \frac{\partial \mathbf{x}_m}{\partial s}(1,0),
\end{aligned} \tag{13}$$

see Fig. 3(d). The edge vectors form the corresponding edge strains,

$$\begin{aligned}
&e^m_{rr}(0,1) = \mathbf{x}^1_e \cdot \mathbf{u}^1_e, \quad e^m_{rr}(0,-1) = \mathbf{x}^3_e \cdot \mathbf{u}^3_e, \quad e^m_{ss}(1,0) = \mathbf{x}^4_e \cdot \mathbf{u}^4_e,\\
&e^m_{ss}(-1,0) = \mathbf{x}^2_e \cdot \mathbf{u}^2_e,
\end{aligned} \tag{14}$$

in which each strain contains only two nodal displacements.

In the original displacement-based element formulation, the displacements at the four nodes give the 'rr'- and 'ss'- membrane strains. However, constraints arise from the condition that the membrane strains should vanish in pure bending situations. The use of the edge strains in Eq. (14) is important to establish an improved behavior in bending-dominated problems [1,23–25,27].

The membrane strains in Eq. (7b) can be expressed using the characteristic geometry and displacement vectors

$$\begin{aligned}
e^m_{rr} &= e^m_{rr}|_{\text{con.}} + e^m_{rr}|_{\text{lin.}} \cdot s + e^m_{rs}|_{\text{bil.}} \cdot s^2,\\
e^m_{ss} &= e^m_{ss}|_{\text{con.}} + e^m_{ss}|_{\text{lin.}} \cdot r + e^m_{rs}|_{\text{bil.}} \cdot r^2,\\
e^m_{rs} &= e^m_{rs}|_{\text{con.}} + \frac{1}{2}e^m_{rr}|_{\text{lin.}} \cdot r + \frac{1}{2}e^m_{ss}|_{\text{lin.}} \cdot s + e^m_{rs}|_{\text{bil.}} \cdot rs
\end{aligned} \tag{15}$$

with

$$\begin{aligned}
&e^m_{rr}|_{\text{con.}} = \mathbf{x}_r \cdot \mathbf{u}_r, e^m_{ss}|_{\text{con.}} = \mathbf{x}_s \cdot \mathbf{u}_s, \quad e^m_{rs}|_{\text{con.}} = \frac{1}{2}(\mathbf{x}_r \cdot \mathbf{u}_s + \mathbf{x}_s \cdot \mathbf{u}_r),\\
&e^m_{rr}|_{\text{lin.}} = \mathbf{x}_r \cdot \mathbf{u}_d + \mathbf{x}_d \cdot \mathbf{u}_r, \quad e^m_{ss}|_{\text{lin.}} = \mathbf{x}_s \cdot \mathbf{u}_d + \mathbf{x}_d \cdot \mathbf{u}_s, e^m_{rs}|_{\text{bil.}} = \mathbf{x}_d \cdot \mathbf{u}_d.
\end{aligned} \tag{16}$$

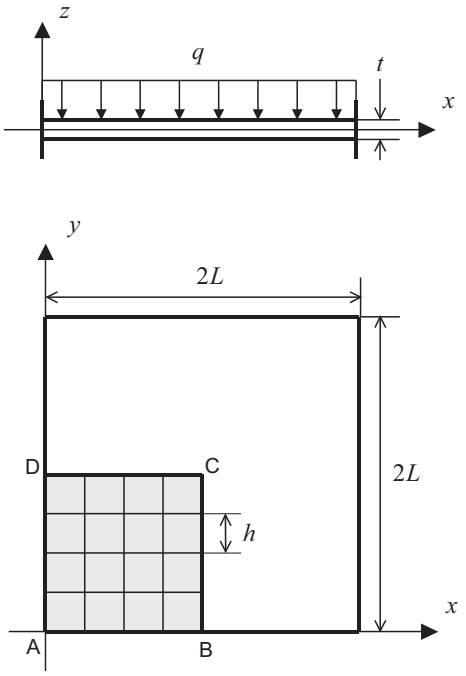

Fig. 6. Fully clamped square plate under uniform pressure ($L = 1.0, E = 1.7472 \times 10^7, q = 1.0$ and $\nu = 0.3$).

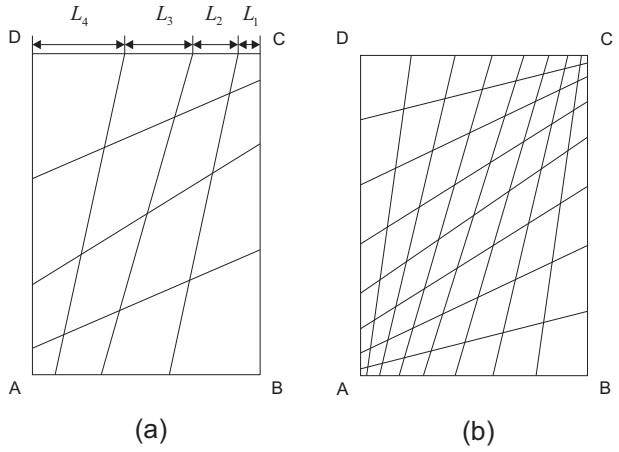

Fig. 7. Distorted mesh patterns for (a) $N = 4$ and (b) $N = 8$.

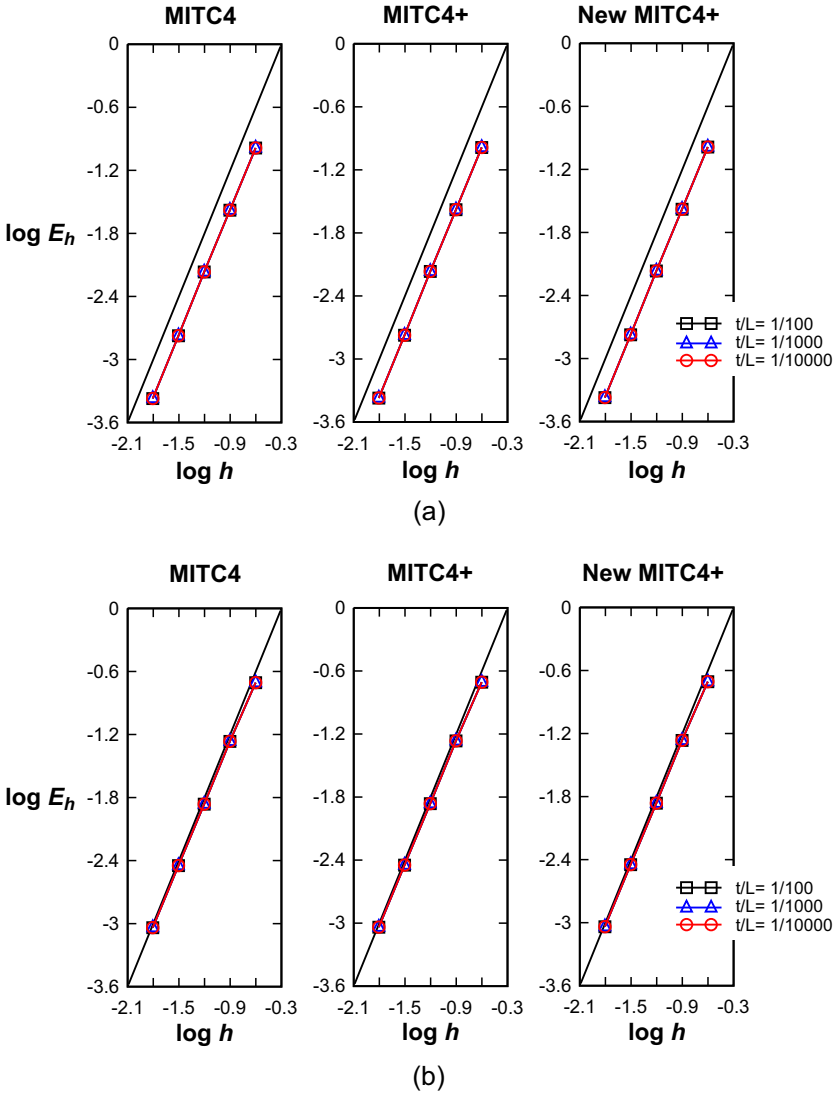

Fig. 8. Convergence curves for the fully clamped square plate problem with (a) the regular and (b) distorted meshes shown in Fig. 7. The bold line represents the optimal convergence rate.

in which the subscripts 'con.', 'lin.' and 'bil.' denote constant, linear and bilinear terms, respectively.

3.2. Construction of the assumed membrane strain field

The following five strain components obtained at tying points are used to construct the assumed membrane strain field [1,23–25]

$$
\begin{aligned}
e_{rr}^{m(A)} &= e_{rr}^{m}(0,1) = e_{rr}^{m}|_{\text{con.}} + e_{rr}^{m}|_{\text{lin.}} + e_{rs}^{m}|_{\text{bil.}},\\
e_{rr}^{m(B)} &= e_{rr}^{m}(0,-1) = e_{rr}^{m}|_{\text{con.}} - e_{rr}^{m}|_{\text{lin.}} + e_{rs}^{m}|_{\text{bil.}},\\
e_{ss}^{m(C)} &= e_{ss}^{m}(1,0) = e_{ss}^{m}|_{\text{con.}} + e_{ss}^{m}|_{\text{lin.}} + e_{rs}^{m}|_{\text{bil.}},\\
e_{ss}^{m(D)} &= e_{ss}^{m}(-1,0) = e_{ss}^{m}|_{\text{con.}} - e_{ss}^{m}|_{\text{lin.}} + e_{rs}^{m}|_{\text{bil.}},\\
e_{rs}^{m(E)} &= e_{rs}^{m}(0,0) = e_{rs}^{m}|_{\text{con.}},
\end{aligned}
\tag{17}
$$

which are effective to reduce membrane locking. The tying points (A)–(E) as well as the corresponding strain components are shown in Fig. 4.

We are particularly interested in the assumed membrane strain field proposed by Choi and Paik [23], which was subsequently applied to an exact geometry shell element by Cho and Roh [24]

$$
\begin{aligned}
\bar{e}_{rr}^{m} &= \frac{1}{2}(e_{rr}^{m(A)} + e_{rr}^{m(B)}) + \frac{1}{2}(e_{rr}^{m(A)} - e_{rr}^{m(B)})\cdot s = (e_{rr}^{m}|_{\text{con.}} + e_{rs}^{m}|_{\text{bil.}}) + e_{rr}^{m}|_{\text{lin.}}\cdot s,\\
\bar{e}_{ss}^{m} &= \frac{1}{2}(e_{ss}^{m(C)} + e_{ss}^{m(D)}) + \frac{1}{2}(e_{ss}^{m(C)} - e_{ss}^{m(D)})\cdot r = (e_{ss}^{m}|_{\text{con.}} + e_{rs}^{m}|_{\text{bil.}}) + e_{ss}^{m}|_{\text{lin.}}\cdot r,\\
\bar{e}_{rs}^{m} &= e_{rs}^{m(E)} = e_{rs}^{m}|_{\text{con.}}.
\end{aligned}
\tag{18}
$$

We add linear terms in the covariant in-plane shear strain in Eq. (18) and obtain the following assumed membrane strain field

$$
\hat{e}_{rr}^{m} = \bar{e}_{rr}^{m},\quad \hat{e}_{ss}^{m} = \bar{e}_{ss}^{m},\quad \hat{e}_{rs}^{m} = \bar{e}_{rs}^{m} + \frac{1}{2}e_{rr}^{m}|_{\text{lin.}}\cdot r + \frac{1}{2}e_{ss}^{m}|_{\text{lin.}}\cdot s, \tag{19}
$$

which is necessary for the shell element to pass the patch test. Then, the five sampled strains in Eq. (17) are used to assume the membrane strain field to be one order lower than implicitly given in the original displacement-based element.

Comparing the strain field in Eq. (19) with the strain field of the displacement-based element (given in Eq. (15)), we can identify the following relations

$$
\begin{aligned}
e_{rr}^{m} &= \hat{e}_{rr}^{m} - e_{rs}^{m}|_{\text{bil.}} + e_{rs}^{m}|_{\text{bil.}}\cdot s^2,\\
e_{ss}^{m} &= \hat{e}_{ss}^{m} - e_{rs}^{m}|_{\text{bil.}} + e_{rs}^{m}|_{\text{bil.}}\cdot r^2,\quad e_{rs}^{m} = \hat{e}_{rs}^{m} + e_{rs}^{m}|_{\text{bil.}}\cdot rs,
\end{aligned}
\tag{20}
$$

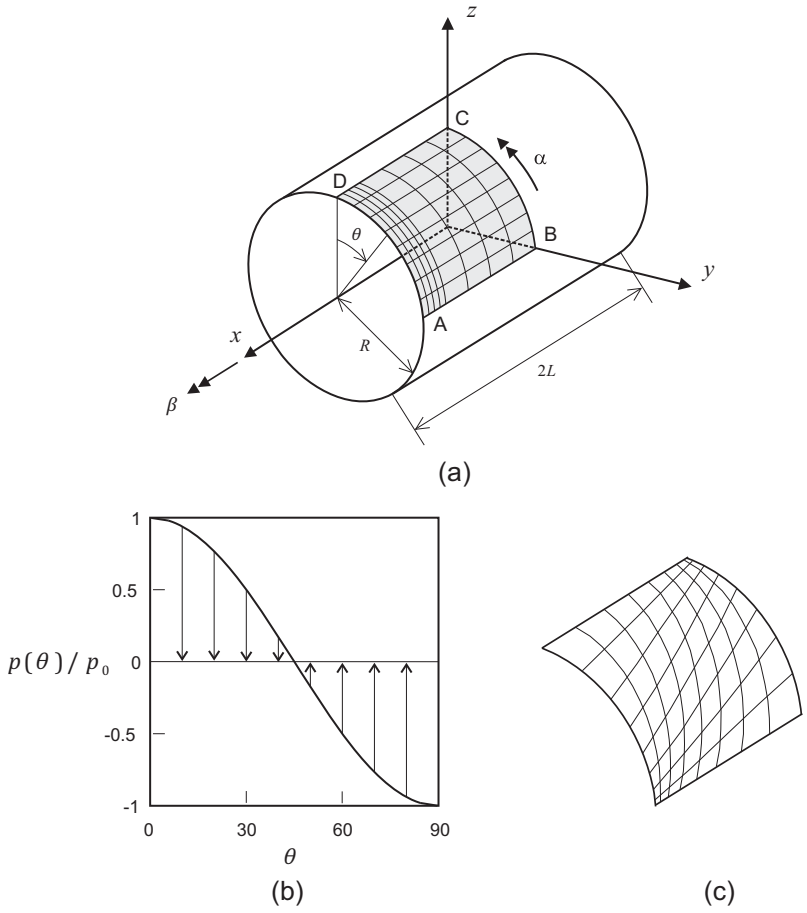

Fig. 9. Cylindrical shell problem ($L = R = 1.0, E = 2.0 \times 10^5, \nu = 1/3$ and $p_0 = 1.0$). (a) Problem description with the graded regular mesh for the clamped case (8×8 mesh, $t/L = 1/100$). (b) Pressure loading. (c) Distorted mesh in Fig. 7 applied.

and we can see that the strain components added to the strain field in Eq. (19) (to complete the strain field of the displacement-based element) cause membrane locking. It is important to note that all the added strain components contain the same term, $e^m_{rs}|_{\text{bil.}} = \mathbf{x}_d \cdot \mathbf{u}_d$ (given in Eq. (16)).

In order to establish an appropriate value for $e^m_{rs}|_{\text{bil.}}$, we adopt the idea of Kulikov and Plotnikova [25]. The assumed membrane strain field is constructed by the linear combination of the five strain coefficients in Eq. (18) such as to keep the improved bending performance with the membrane locking alleviated

$$\begin{aligned}\tilde{e}^m_{rs}|_{\text{bil.}} &= B_1 \cdot (e^m_{rr}|_{\text{con.}} + e^m_{rs}|_{\text{bil.}}) + B_2 \cdot (e^m_{ss}|_{\text{con.}} + e^m_{rs}|_{\text{bil.}}) \\ &\quad + B_3 \cdot e^m_{rs}|_{\text{con.}} + B_4 \cdot e^m_{rr}|_{\text{lin.}} + B_5 \cdot e^m_{ss}|_{\text{lin.}},\end{aligned} \tag{21}$$

where the constants $(B_1, B_2, B_3, B_4$ and $B_5)$ need to be determined. Note that the five strain coefficients can be easily obtained from the sampled strain components in Eq. (17).

To pass the membrane patch tests, the new membrane strain field should satisfy the following condition:

$$\tilde{e}^m_{rs}|_{\text{bil.}} = e^m_{rs}|_{\text{bil.}} \quad \text{when the element geometry is flat } (\mathbf{x}_d \cdot \mathbf{n} = 0) \tag{22}$$

for arbitrary in-plane deformation modes in the flat geometry.

For a flat element geometry with $\mathbf{x}_d \cdot \mathbf{n} = 0$ in the plane P defined in Eq. (10), the distortion vector in Eq. (12) becomes

$$\mathbf{x}_d = (\mathbf{x}_d \cdot \mathbf{m}^r)\mathbf{x}_r + (\mathbf{x}_d \cdot \mathbf{m}^s)\mathbf{x}_s. \tag{23}$$

Solving Eq. (22) for arbitrary in-plane modes with Eq. (23), the five constants in Eq. (21) are determined, see Appendix A,

$$B_1 = c_r^2/d, \quad B_2 = c_s^2/d, \quad B_3 = 2c_r c_s/d, \quad B_4 = -c_r/d, \quad B_5 = -c_s/d, \tag{24}$$

with

$$c_r = \mathbf{x}_d \cdot \mathbf{m}^r, \quad c_s = \mathbf{x}_d \cdot \mathbf{m}^s,$$
$$d = c_r^2 + c_s^2 - 1 = (\mathbf{x}_e^2 \cdot \mathbf{m}^s)(\mathbf{x}_e^4 \cdot \mathbf{m}^s) + (\mathbf{x}_e^3 \cdot \mathbf{m}^r)(\mathbf{x}_e^1 \cdot \mathbf{m}^r) + 1,$$

in which c_r and c_s denote the in-plane distortions in Eq. (23) and d measures the distortion of pairs of edges within the element and is only equal to zero when the element is extremely distorted. Hence we assume in the following that d is not zero.

Then, the assumed membrane strain term for $\tilde{e}^m_{rs}|_{\text{bil.}}$ is given by

$$\begin{aligned}\tilde{e}^m_{rs}|_{\text{bil.}} &= \frac{c_r}{d}\left[c_r(e^m_{rr}|_{\text{con.}} + e^m_{rs}|_{\text{bil.}}) - e^m_{rr}|_{\text{lin.}}\right] \\ &\quad + \frac{c_s}{d}\left[c_s(e^m_{ss}|_{\text{con.}} + e^m_{rs}|_{\text{bil.}}) - e^m_{ss}|_{\text{lin.}}\right] + \frac{2c_r c_s}{d} e^m_{rs}|_{\text{con.}}.\end{aligned} \tag{25}$$

Substituting this assumed strain term into all added strain components in Eq. (20), we finally obtain the new assumed membrane strain field for the 4-node continuum mechanics based shell element,

$$\begin{aligned}&\tilde{e}^m_{rr} = \hat{e}^m_{rr} - \tilde{e}^m_{rs}|_{\text{bil.}} + \tilde{e}^m_{rs}|_{\text{bil.}} \cdot s^2, \quad \tilde{e}^m_{ss} = \hat{e}^m_{ss} - \tilde{e}^m_{rs}|_{\text{bil.}} + \tilde{e}^m_{rs}|_{\text{bil.}} \cdot r^2, \\ &\tilde{e}^m_{rs} = \hat{e}^m_{rs} + \tilde{e}^m_{rs}|_{\text{bil.}} \cdot rs.\end{aligned} \tag{26}$$

For an efficient implementation in computer codes, the assumed strain field in Eq. (26) can be rewritten as

$$\begin{aligned}\tilde{e}^m_{rr} = &\frac{1}{2}(1 - 2a_A + s + 2a_A \cdot s^2)e^{m(A)}_{rr} + \frac{1}{2}(1 - 2a_B - s + 2a_B \cdot s^2)e^{m(B)}_{rr} \\ &+ a_C(-1 + s^2)e^{m(C)}_{ss} + a_D(-1 + s^2)e^{m(D)}_{ss} + a_E(-1 + s^2)e^{m(E)}_{rs},\end{aligned} \tag{27a}$$

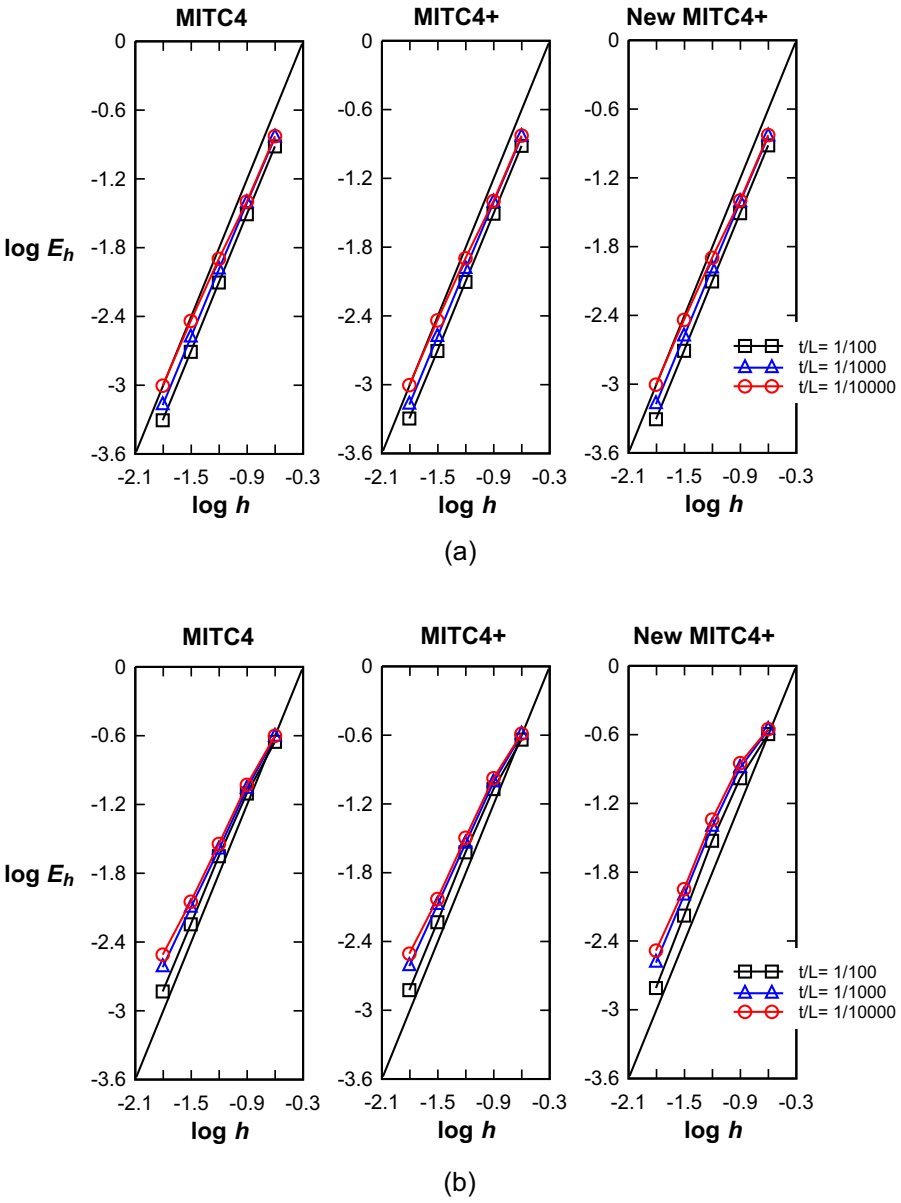

Fig. 10. Convergence curves for the clamped cylindrical shell problem with (a) the graded regular or (b) distorted meshes. The bold line represents the optimal convergence rate.

$$\tilde{e}^m_{ss} = a_A(-1+r^2)\,e^{m(A)}_{rr} + a_B(-1+r^2)\,e^{m(B)}_{rr} + \frac{1}{2}(1-2a_C+r + 2a_C\cdot r^2)\,e^{m(C)}_{ss} + \frac{1}{2}(1-2a_D-r+2a_D\cdot r^2)\,e^{m(D)}_{ss} + a_E(-1+r^2)\,e^{m(E)}_{rs}, \tag{27b}$$

$$\tilde{e}^m_{rs} = \frac{1}{4}(r+4a_A\cdot rs)\,e^{m(A)}_{rr} + \frac{1}{4}(-r+4a_B\cdot rs)\,e^{m(B)}_{rr} + \frac{1}{4}(s+4a_C\cdot rs)\,e^{m(C)}_{ss} + \frac{1}{4}(-s+4a_D\cdot rs)\,e^{m(D)}_{ss} + (1+a_E\cdot rs)\,e^{m(E)}_{rs}, \tag{27c}$$

with

$$a_A = \frac{c_r(c_r-1)}{2d}, \quad a_B = \frac{c_r(c_r+1)}{2d}, \quad a_C = \frac{c_s(c_s-1)}{2d}, \quad a_D = \frac{c_s(c_s+1)}{2d}, \quad a_E = \frac{2c_rc_s}{d}.$$

We note that the membrane part of the new MITC4+ shell element is identical to that of the displacement-based element when the element geometry is flat. That is, in two-dimensional plane stress problems, both shell elements always yield the identical solutions. We also note that the computational cost of the new MITC4+ shell element is only somewhat higher than that of the original MITC4 shell element.

In the numerical solutions, we use $2\times2\times2$ Gauss integration over the element domain for all shell elements considered.

In this section, we have developed the formulation of a new generally applicable continuum mechanics based shell element. We illustrate the excellent performance of the new MITC4+ shell element in the next sections.

4. Basic numerical tests

We note that the element formulation does not include any numerical factor, and consider next the isotropy, zero energy mode and patch tests.

The spatially isotropic behavior is an important requirement for any shell element. The element behavior should not depend on the

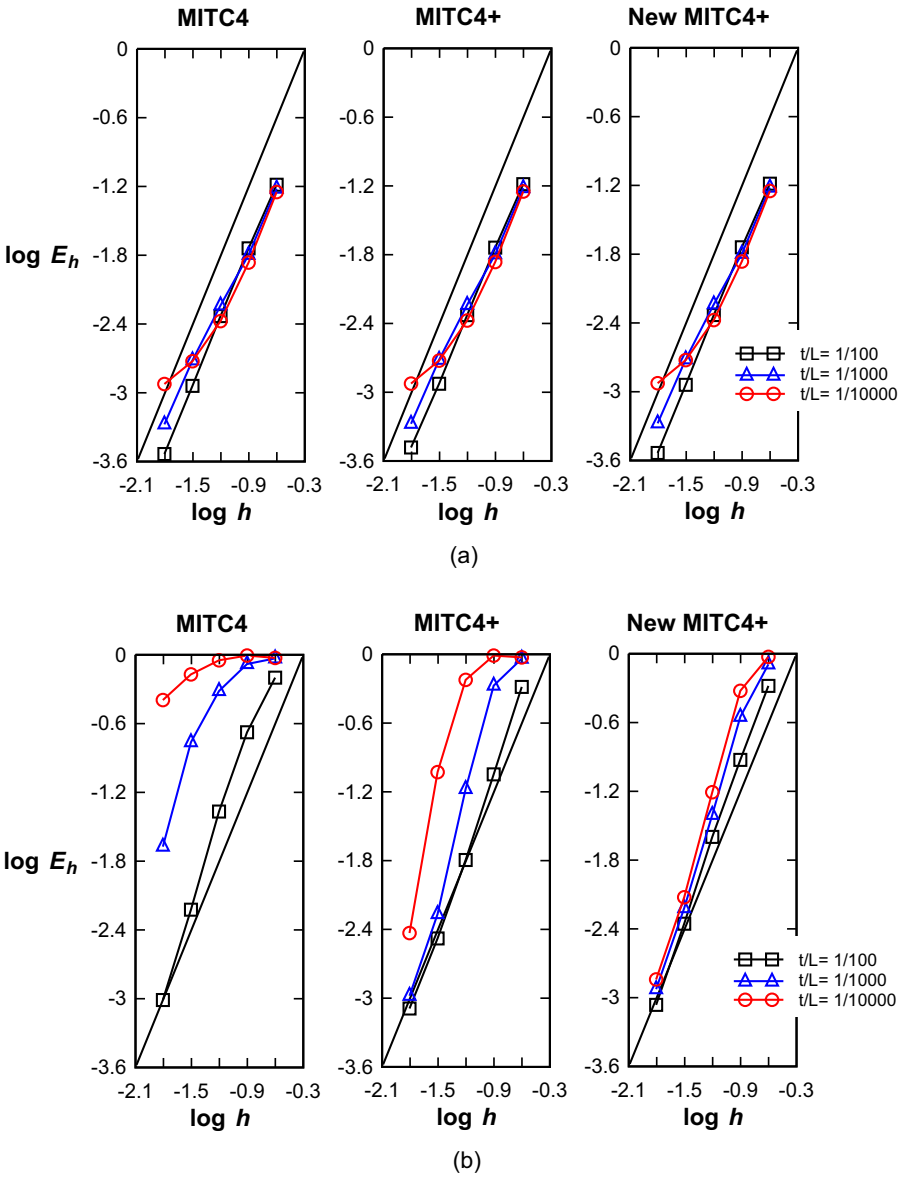

Fig. 11. Convergence curves for the free cylindrical shell problem with (a) the regular and (b) distorted meshes. The bold line represents the optimal convergence rate.

sequence of node numbering, i.e. on the element orientation [1,3,15–18]. The element passes the test of spatial isotropy.

In the zero energy mode test, the number of zero eigenvalues of the stiffness matrix of a single unsupported element are counted [1–3,9–18]. For the new element only the six zero eigenvalues corresponding to the six rigid body modes are obtained. That is, the element passes the zero energy mode test.

We perform three patch tests: the membrane, bending and shearing patch tests, see Refs. [1–3,9–18] for the patch tests. The mesh geometry is shown in Fig. 5. The patch of elements is subjected to the minimum number of constrains to prevent rigid body motions and the nodal point forces on the boundary corresponding to the constant stress states are applied. The patch tests are passed if the correct values of constant stress fields are calculated at any location within the mesh. The element passes the membrane, bending and shearing patch tests.

5. Convergence studies

In this section, we perform convergence studies using appropriate and well-established benchmark problems to study the behavior of shell elements: a clamped square plate problem, and cylindrical, hyperboloid and spherical shell problems [1,5–11,13,14–17,24,26,28–32]. We note that the chosen problems are behavior-encompassing, in that the typical shell behaviors encountered in shell analyses are considered.

We measure the solution errors in an appropriate norm considering membrane and bending-dominated shell problems with various curvatures, thicknesses, and boundary conditions.

To measure the error in the finite element solution, we use the s-norm proposed by Hiller and Bathe [29]

$$\|\mathbf{u}-\mathbf{u}_h\|_s^2 = \int_\Omega \Delta\boldsymbol{\varepsilon}^T \Delta\boldsymbol{\tau} d\Omega \quad \text{with } \Delta\boldsymbol{\varepsilon} = \boldsymbol{\varepsilon} - \boldsymbol{\varepsilon}_h, \Delta\boldsymbol{\tau} = \boldsymbol{\tau} - \boldsymbol{\tau}_h, \tag{28}$$

where $\mathbf{u}$ is the exact solution, $\mathbf{u}_h$ is the solution of the finite element discretization, and $\boldsymbol{\varepsilon}$ and $\boldsymbol{\tau}$ are the strain and stress vectors. This is a proper norm for investigating whether a finite element formulation satisfies the consistency and inf-sup conditions [3–5,13–18,29,30].

Since many good benchmark shell problems designed to detect locking have no analytical solution, an accurate finite element solution using a very fine mesh $\mathbf{u}_{ref}$ is used to replace the exact solution $\mathbf{u}$. Hence the s-norm in Eq. (28) is modified to be

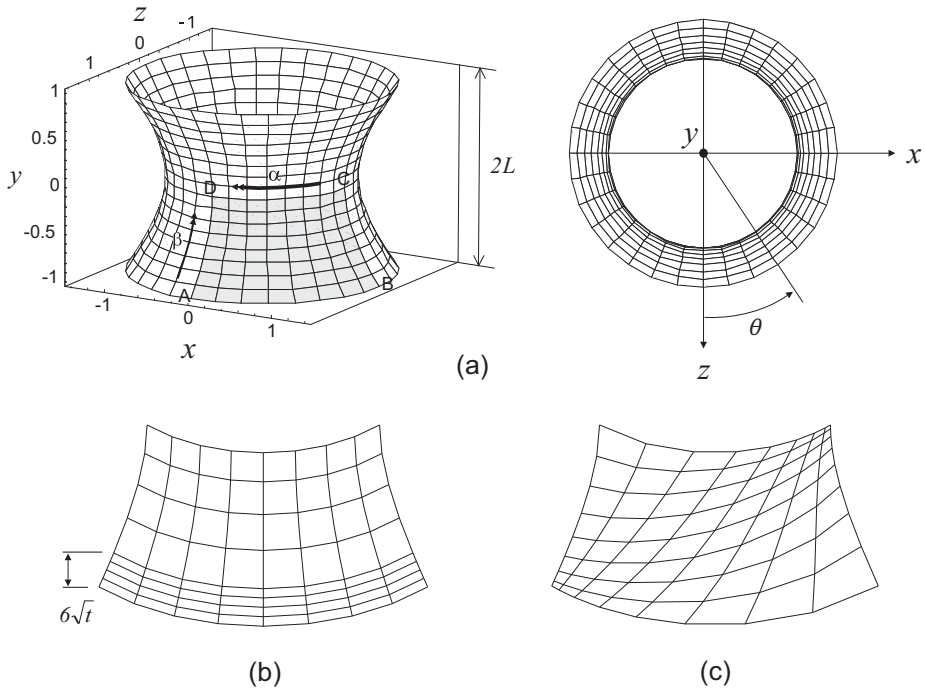

Fig. 12. Hyperboloid shell problem ($E = 2.0 \times 10^{11}, \nu = 1/3, L = 1.0$ and $p_0 = 1.0$). (a) Problem description. (b) Graded regular mesh for the clamped case (8×8 mesh, $t/L = 1/1000$). (c) Distorted mesh in Fig. 7 applied.

$$\|\mathbf{u}_{ref} - \mathbf{u}_h\|_s^2 = \int_{\Omega_{ref}} \Delta\boldsymbol{\varepsilon}^T \Delta\boldsymbol{\tau} d\Omega_{ref} \quad \text{with } \Delta\boldsymbol{\varepsilon} = \boldsymbol{\varepsilon}_{ref} - \boldsymbol{\varepsilon}_h, \quad \Delta\boldsymbol{\tau} = \boldsymbol{\tau}_{ref} - \boldsymbol{\tau}_h. \tag{29}$$

To study the solution convergence of shell finite elements with decreasing shell thicknesses, we use the normalized relative error E_h

$$E_h = \frac{\|\mathbf{u}_{ref} - \mathbf{u}_h\|_s^2}{\|\mathbf{u}_{ref}\|_s^2}. \tag{30}$$

The theoretical convergence behavior, which corresponds to the optimal convergence, is given by

$$E_h \cong Ch^k, \tag{31}$$

in which C is a constant independent of the shell thickness and h is the element size. For 4-node shell elements, $k = 2$.

In this study, well-converged reference solutions calculated using fine regular meshes of the MITC9 shell elements are used. The MITC9 shell element is known to satisfy the ellipticity and consistency conditions and to show good convergence behaviors [3–6,10,13,28–30].

In each of the problem analyses we give the results obtained using the classical MITC4 shell element, the previously published and the new MITC4+ shell elements, and we show how the results change as the thickness of the shell decreases. Also, uniformly regular and distorted meshes are used.

5.1. Fully clamped square plate problem

The plate bending problem [1,5,11,14–17,30,31] shown in Fig. 6 is considered. A square plate of dimensions $2L \times 2L$ and uniform thickness t is subjected to a uniform pressure. Utilizing the symmetry condition, only a one-quarter model is considered, with the following boundary conditions: $u_x = \theta_y = 0$ along BC, $u_y = \theta_x = 0$ along DC and $u_x = u_y = u_z = \theta_x = \theta_y = 0$ along AB and AD. In addition to the regular mesh in Fig. 6, we consider the same plate bending problem with distorted meshes shown in Fig. 7. Then, when we use an $N \times N$ element mesh, each edge is discretized in the following ratio: $L_1{:}L_2{:}L_3{:}\ldots L_N = 1{:}2{:}3{:}\ldots N$.

Fig. 8 gives the convergence curves of the three shell elements. A 72×72 element mesh of MITC9 shell elements is used to obtain the reference solution. We use $N \times N$ element meshes ($N = 4$, 8, 16, 32, and 64) to calculate the solutions. The element size in the convergence curves is $h = L/N$. The performance of the elements is uniformly optimal in both the regular and distorted meshes. Note that membrane locking is inherently not present in this plate bending problem.

5.2. Cylindrical shell problems

We consider the cylindrical shell of length $2L$, radius R and uniform thickness t as shown in Fig. 9(a), see Refs. [1,5–7,15–17,26,28]. The loading is a smoothly varying pressure $p(\theta)$

$$p(\theta) = p_0 \cos(2\theta), \tag{32}$$

see Fig. 9(b).

This shell structure shows two different asymptotic behaviors depending on the boundary conditions at its ends: bending-dominated behavior when both ends are free and membrane-dominated behavior when both ends are clamped.

Using symmetry, only the region ABCD in Fig. 9(a) is modeled. For the membrane-dominated case, the clamped boundary condition is imposed: $u_z = \beta = 0$ along AB, $u_y = \beta = 0$ along DC, and $u_x = \alpha = 0$ along BC, and $u_x = u_y = u_z = \alpha = \beta = 0$ along AD. For the bending-dominated case, the free boundary condition is imposed: $u_z = \beta = 0$ along AB, $u_y = \beta = 0$ along DC, and $u_x = \alpha = 0$ along BC. When using the clamped boundary condition, the regular mesh is graded with a boundary layer of width $2\sqrt{t}$, see Refs. [1,6,28] for details. In the free boundary condition, the graded mesh with a boundary layer of width $0.5\sqrt{t}$ is considered [1,6]. We also perform the convergence studies with the distorted meshes shown in Fig. 9(c).

Fig. 10 gives the convergence curves in the solution of the clamped cylindrical shell problems. The reference solutions are cal-

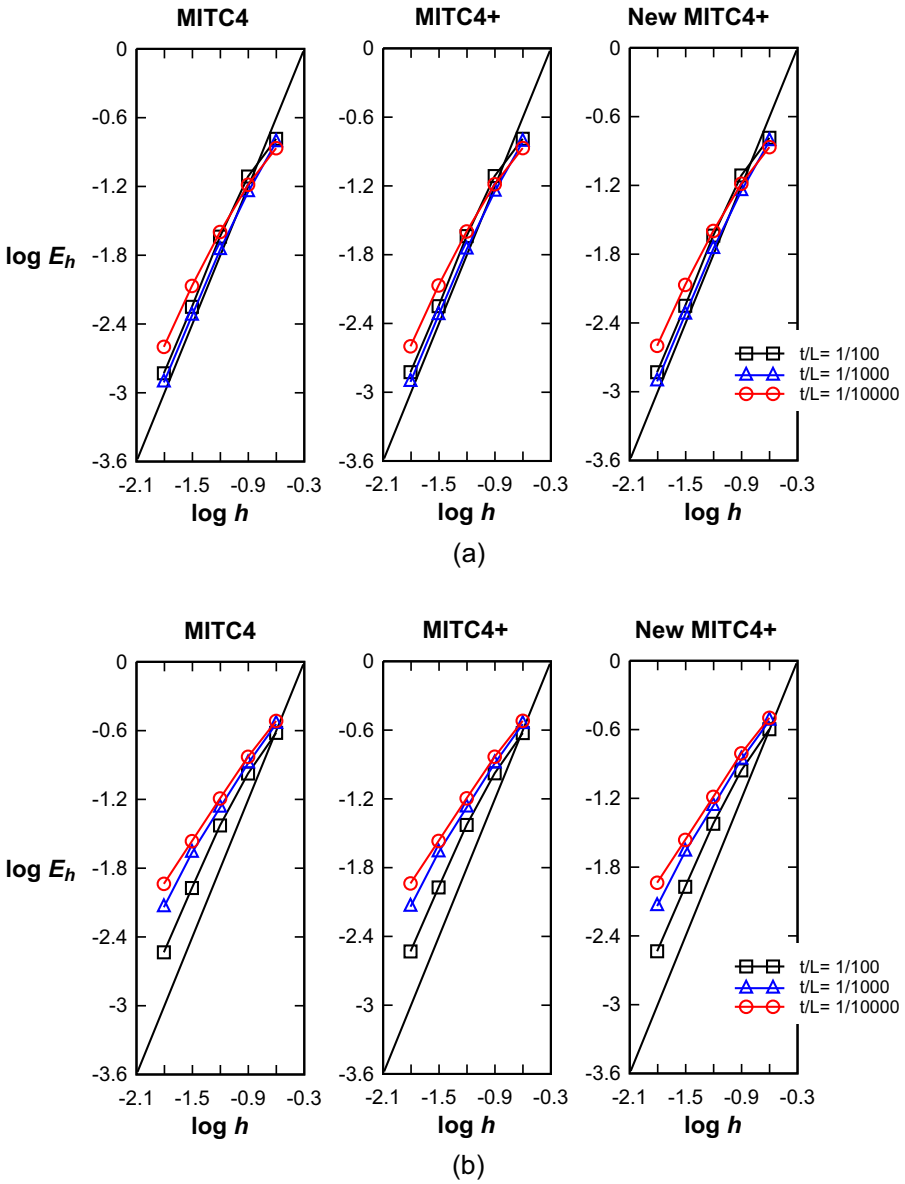

Fig. 13. Convergence curves for the clamped hyperboloid shell problem with (a) the graded regular and (b) distorted meshes. The bold line represents the optimal convergence rate.

culated using a 72×72 element mesh of MITC9 shell elements. The solutions are obtained with $N \times N$ element meshes ($N = 4$, 8, 16, 32, and 64). The element size is $h = L/N$. In this problem, all shell elements present similarly good convergence behaviors.

Fig. 11 shows the convergence curves for the free cylindrical shell problems. Note that, in the regular meshes, all 4-node shell elements have a flat geometry, and thus membrane locking does not occur. However, in the distorted meshes, the element geometry is not flat, which induces membrane locking. In those cases, the performance of the MITC4 shell element severely deteriorates. The new MITC4+ shell element shows an excellent performance.

5.3. Hyperboloid shell problems

Here, the hyperboloid shell shown in Fig. 12(a) is considered, see Refs. [1,5,6,13,14–17,26,29]. The mid-surface of the shell structure is given by

$$x^2 + z^2 = 1 + y^2; \quad y \in [-1, \quad 1]. \tag{33}$$

As for the cylindrical shell problems, a smoothly varying pressure in Eq. (32) is applied.

A bending-dominated behavior is obtained with free ends and a membrane-dominated behavior is given with clamped ends, similar to the cases of the cylindrical shell.

Due to symmetry, only one-eighth of the structure corresponding to the shaded region ABCD in Fig. 12(a) is modeled for the analysis. For the membrane-dominated case, the clamped boundary condition is imposed: $u_z = \beta = 0$ along BC, $u_x = \beta = 0$ along AD, $u_y = \alpha = 0$ along DC, and $u_x = u_y = u_z = \alpha = \beta = 0$ along AB. For the bending-dominated case, the free boundary condition is imposed: $u_z = \beta = 0$ along BC, $u_x = \beta = 0$ along AD, and $u_y = \alpha = 0$ along DC.

In both cases, a 72×72 element mesh of MITC9 shell elements is used to obtain the reference solutions. The solutions are calculated using $N \times N$ element meshes ($N = 4$, 8, 16, 32 and 64). The element size is $h = L/N$. For the clamped boundary condition, the regular mesh graded in a boundary layer of width $6\sqrt{t}$ shown in Fig. 12(b) is considered, see Refs. [1,6,13,14–17,29]. For the free boundary condition, the regular mesh is graded in a boundary layer

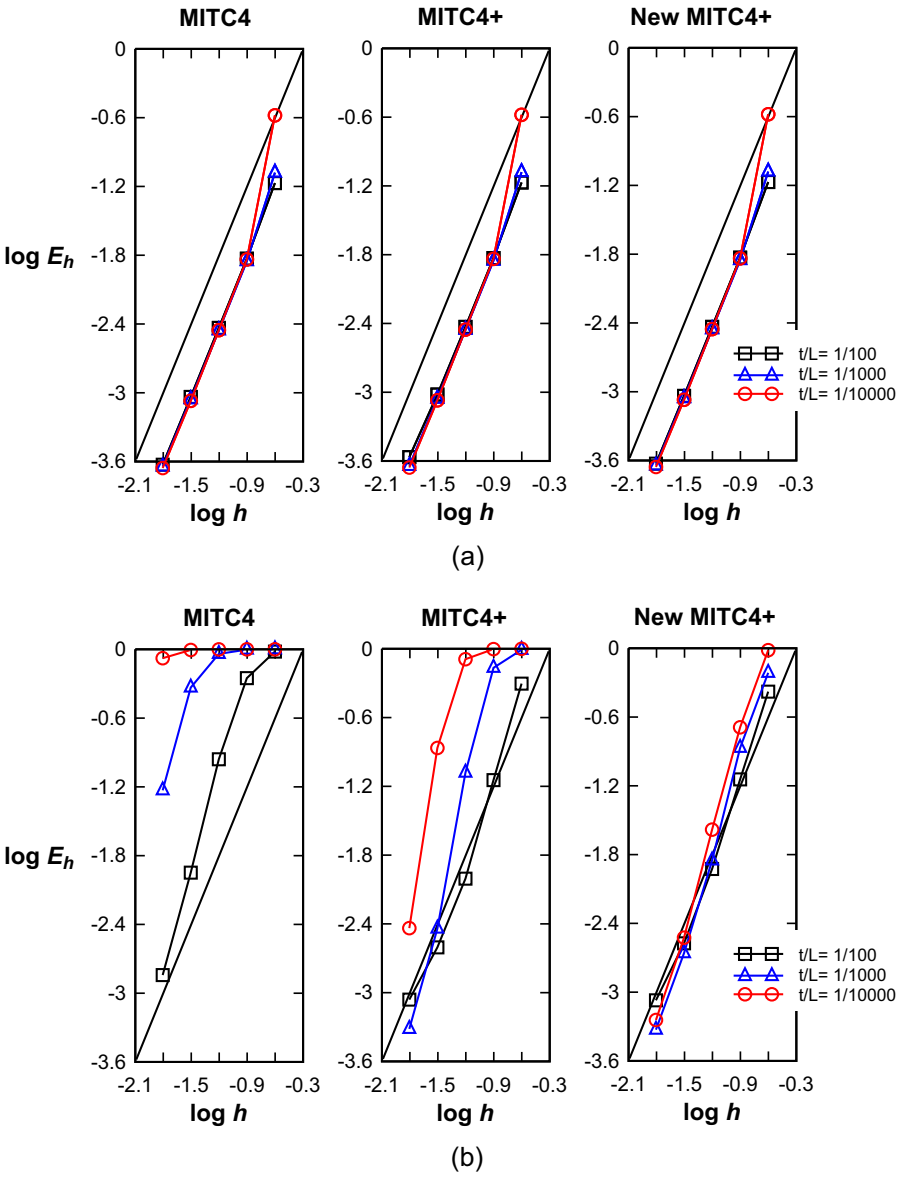

Fig. 14. Convergence curves for the free hyperboloid shell problem with (a) the regular and (b) distorted meshes. The bold line represents the optimal convergence rate.

of width $0.5\sqrt{t}$ [1,6,13,14,29]. We also perform the convergence studies with the distorted meshes shown in Fig. 12(c).

Fig. 13 shows the good convergence behavior of all elements in the solution of the clamped hyperboloid shell problem. Fig. 14 shows the convergence curves for the solution of the free hyperboloid shell problem. While all shell elements behave well when using the regular meshes, the convergence behavior of the MITC4 and previously published MITC4+ shell elements deteriorate when using the distorted meshes. However, the new MITC4+ shell element shows an almost uniformly optimal and thus ideal convergence behavior.

5.4. Spherical shell problems

Finally, the spherical shell of radius R shown in Fig. 15(a) is considered. The spherical shell has 18° circular cutouts at its top and bottom. The varying pressure in Eq. (32) with the azimuthal angle θ is applied. The problem geometry is as in Refs. [6,10,11,24,32] but a different loading and different boundary conditions are used.

A bending-dominated behavior is obtained with free ends and a membrane-dominated behavior is given with clamped ends, similar to the cylindrical and hyperboloid shell problems.

Utilizing the symmetry, only one-eighth of the structure corresponding to the shaded region ABCD in Fig. 15(a) is modeled for the analysis. For the membrane-dominated case, the clamped boundary condition is imposed: $u_x = \beta = 0$ along BC, $u_y = \beta = 0$ along AD, $u_z = \alpha = 0$ along AB, and $u_x = u_y = u_z = \alpha = \beta = 0$ along DC. For the bending-dominated case, the free boundary condition is imposed: $u_x = \beta = 0$ along BC, $u_y = \beta = 0$ along AD, and $u_z = \alpha = 0$ along AB. In the free boundary condition, we found by numerical experiments a boundary layer of angle $\varphi_l = 15^\circ$ and hence we use the regular mesh graded in that boundary layer shown in Fig. 15(b). We also perform the convergence studies with the distorted meshes shown in Fig. 15(c).

Fig. 16 presents the convergence curves in the solution of the clamped spherical shell problem. The reference solutions are calculated using a 72×72 element mesh of MITC9 shell elements. The solutions are obtained with $N \times N$ element meshes ($N = 4$, 8,

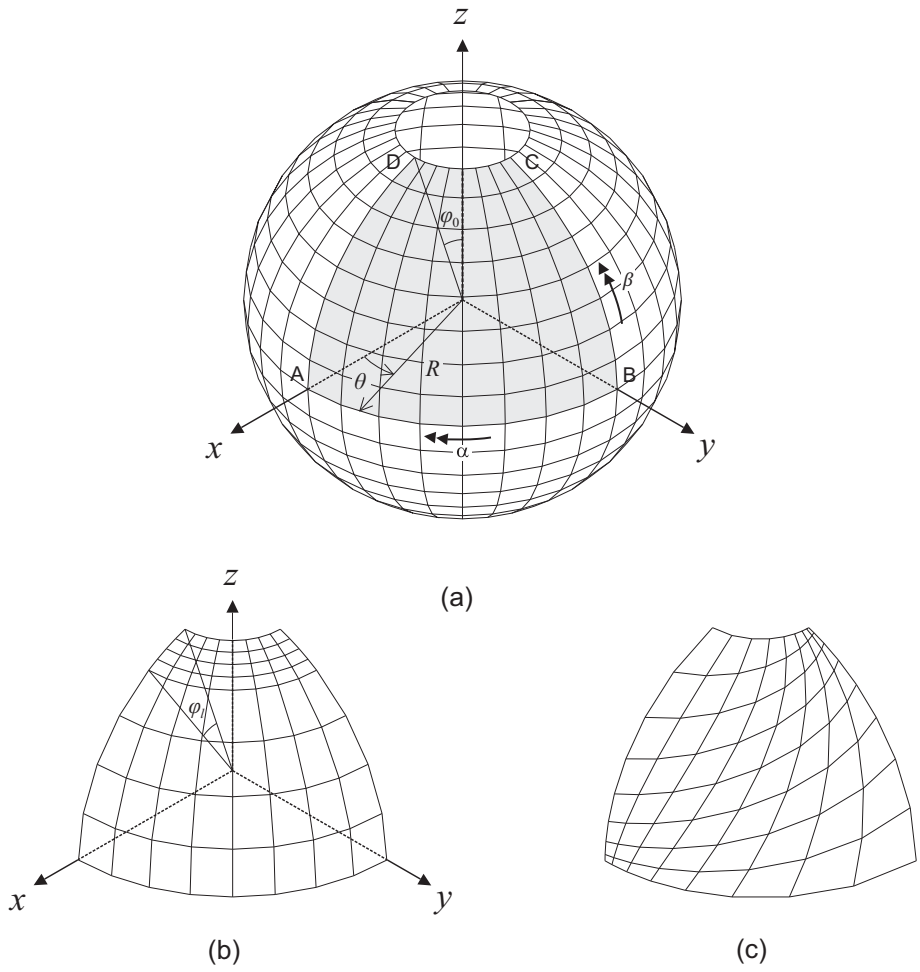

Fig. 15. Spherical shell problem ($E = 2.0 \times 10^{11}, \nu = 1/3, R = 1.0, \varphi_0 = 18^\circ$ and $p_0 = 1.0$). (a) Problem description. (b) Graded regular mesh for the free case (8×8 mesh, $\varphi_l = 15^\circ$). (c) Distorted mesh in Fig. 7 applied.

16, 32, and 64). The element size is $h = L/N$ with $L = R$. All shell elements present similarly good convergence behaviors.

Fig. 17 shows the convergence curves for the free spherical shell problem. In the regular meshes, all elements perform equally and very well. However, in the distorted meshes, the convergence behaviors of the MITC4 and previously published MITC4+ shell elements deteriorate. On the other hand, the new MITC4+ shell element also then shows an excellent performance.

6. Concluding remarks

In this study, we developed a new MITC4+ continuum mechanics-based shell element using the MITC approach to alleviate shear and membrane locking. The shear locking is alleviated by using the interpolations of the classical MITC4 element formulation. The membrane locking is alleviated by the use of characteristic geometry and displacement vectors and using a new MITC interpolation on the membrane strains. The new MITC4+ shell element does not contain an adjustable numerical factor, passes all basic tests and shows in an appropriate norm excellent performance in the solution of membrane and bending-dominated problems even when significantly distorted meshes are used. Indeed, in the difficult to solve elliptic and hyperboloid shell analysis problems the element shows an almost ideal behavior.

The new MITC4+ shell element displays a significantly better behavior than the earlier published MITC4+ shell element, and is computationally more effective. The element is identical to the original MITC4 shell element for a flat geometry and hence the membrane behavior is well preserved. Finally we should note that the given MITC schemes are also applicable in the formulation of solid-shell [32] and 3D-shell elements [33] and in nonlinear analysis [3,34].

Acknowledgments

This research was supported by a grant (MPSS-CG-2016-04) through the Disaster and Safety Management Institute funded by Ministry of Public Safety and Security of Korean government, and the Climate Change Research Hub of KAIST (No. N11160021).

Appendix A. Derivation of the constants in Eq. (24)

Our objective is to determine the constants in Eq. (24).

The term $e^m_{rs}|_{\text{bil.}} = \mathbf{x}_d \cdot \mathbf{u}_d$ should become zero in the following deformation mode

$$\mathbf{u}_r = \mathbf{a}_r, \quad \mathbf{u}_s = \mathbf{a}_s, \quad \mathbf{u}_d = \mathbf{0}, \tag{A.1}$$

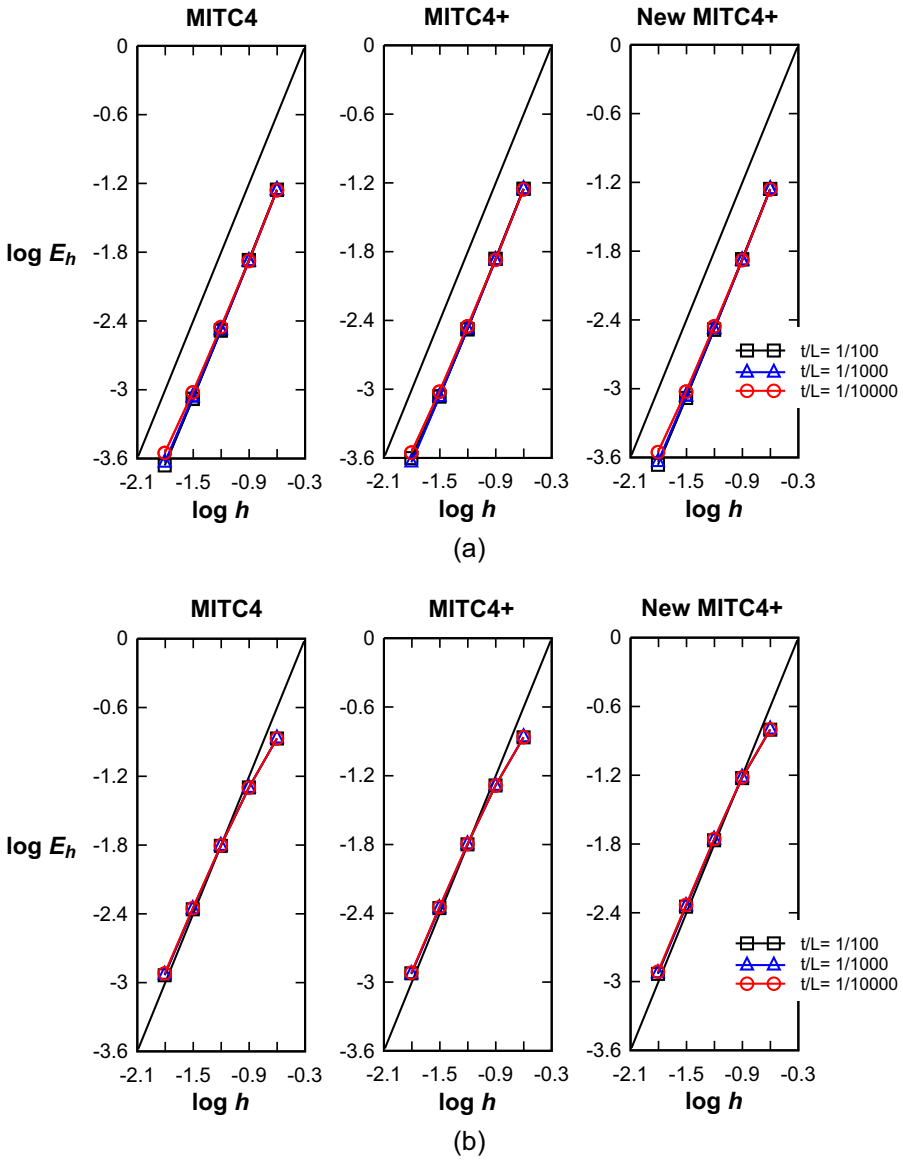

Fig. 16. Convergence curves for the clamped spherical shell problem with (a) the regular and (b) distorted meshes. The bold line represents the optimal convergence rate.

in which $\mathbf{a}_r$ and $\mathbf{a}_s$ are arbitrary constant vectors placed in the plane P. From the condition in Eq. (22), the assumed membrane strain in Eq. (21) also should be zero,

$$\tilde{e}^m_{rs}|_{\text{bil.}} = 0 \tag{A.2}$$

in the deformation mode of Eq. (A.1).

Using Eq. (A.1) in Eq. (16), the five strain coefficients in Eq. (18) become

$$\begin{aligned}
&(e^m_{rr}|_{\text{con.}} + e^m_{rs}|_{\text{bil.}}) = \mathbf{x}_r \cdot \mathbf{a}_r, (e^m_{ss}|_{\text{con.}} + e^m_{rs}|_{\text{bil.}}) = \mathbf{x}_s \cdot \mathbf{a}_s,\\
&e^m_{rs}|_{\text{con.}} = \frac{1}{2}(\mathbf{x}_r \cdot \mathbf{a}_s + \mathbf{x}_s \cdot \mathbf{a}_r),\\
&e^m_{rr}|_{\text{lin.}} = \mathbf{x}_d \cdot \mathbf{a}_r, \quad e^m_{ss}|_{\text{lin.}} = \mathbf{x}_d \cdot \mathbf{a}_s.
\end{aligned} \tag{A.3}$$

Substituting Eqs. (A.2) and (A.3) into Eq. (21), the following equation is obtained

$$(B_1 \cdot \mathbf{x}_r + B_3 \cdot \mathbf{x}_s/2 + B_4 \cdot \mathbf{x}_d) \cdot \mathbf{a}_r + (B_3 \cdot \mathbf{x}_r/2 + B_2 \cdot \mathbf{x}_s + B_5 \cdot \mathbf{x}_d) \cdot \mathbf{a}_s = 0 \tag{A.4}$$

for arbitrary constant vectors $\mathbf{a}_r$ and $\mathbf{a}_s$,

and thus

$$B_1 \cdot \mathbf{x}_r + B_3 \cdot \mathbf{x}_s/2 + B_4 \cdot \mathbf{x}_d = \mathbf{0}, \quad B_3 \cdot \mathbf{x}_r/2 + B_2 \cdot \mathbf{x}_s + B_5 \cdot \mathbf{x}_d = \mathbf{0}. \tag{A.5}$$

Comparing Eq. (A.5) with Eq. (23), we can easily identify

$$B_1 = c_r^2/d, \quad B_2 = c_s^2/d, \quad B_3 = 2c_r c_s/d, \quad B_4 = -c_r/d, \quad B_5 = -c_s/d \tag{A.6}$$

with $c_r = \mathbf{x}_d \cdot \mathbf{m}^r, c_s = \mathbf{x}_d \cdot \mathbf{m}^s$ and a constant d.

We then obtain

$$\begin{aligned}
\tilde{e}^m_{rs}|_{\text{bil.}} = {}& \frac{c_r^2}{d}\left(e^m_{rr}|_{\text{con.}} + e^m_{rs}|_{\text{bil.}}\right) + \frac{c_s^2}{d}\left(e^m_{ss}|_{\text{con.}} + e^m_{rs}|_{\text{bil.}}\right)\\
&+ \frac{2c_r c_s}{d} e^m_{rs}|_{\text{con.}} - \frac{c_r}{d} e^m_{rr}|_{\text{lin.}} - \frac{c_s}{d} e^m_{ss}|_{\text{lin.}}.
\end{aligned} \tag{A.7}$$

We can identify that $e^m_{rs}|_{\text{bil.}} = \mathbf{x}_d \cdot \mathbf{x}_d$ in the following deformation mode

$$\mathbf{u}_r = \mathbf{0}, \quad \mathbf{u}_s = \mathbf{0}, \quad \mathbf{u}_d = \mathbf{x}_d, \tag{A.8}$$

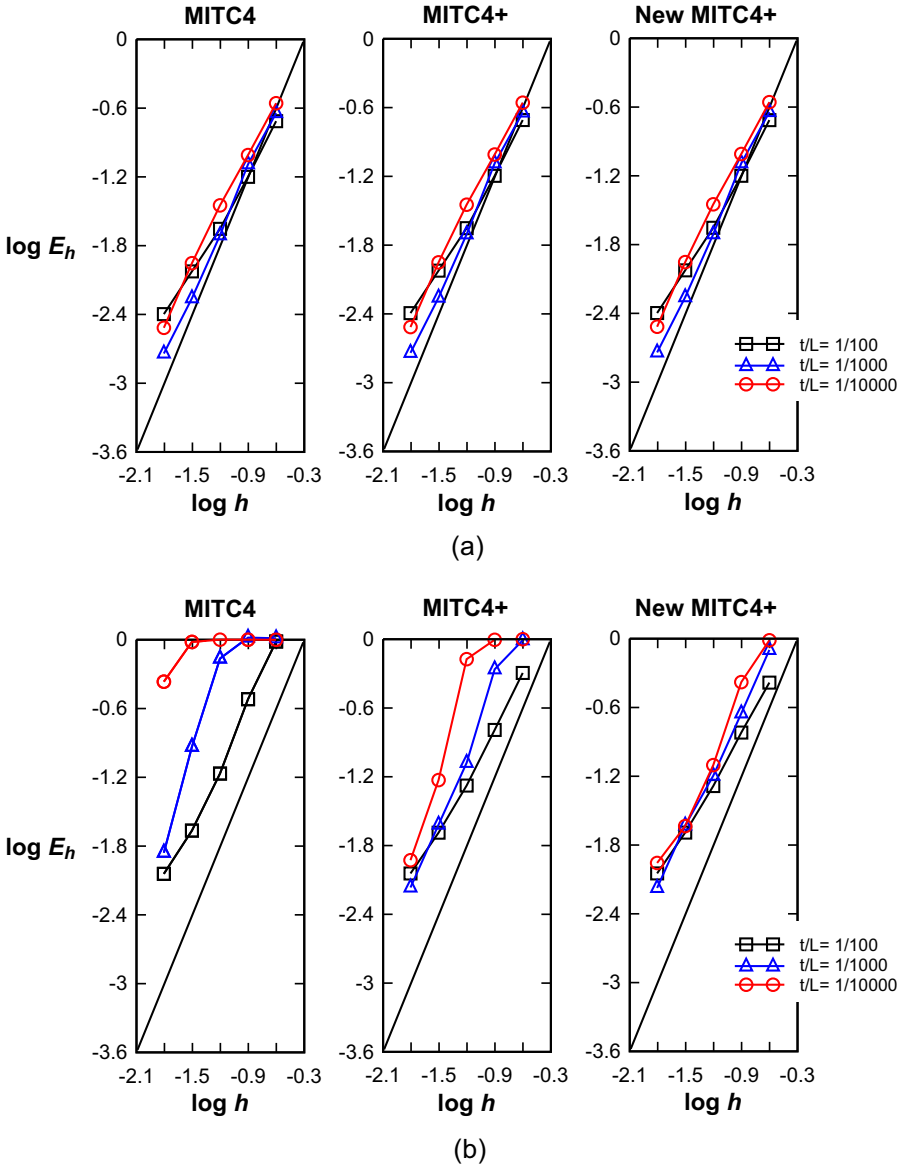

Fig. 17. Convergence curves for the free spherical shell problem with (a) the graded regular and (b) distorted meshes. The bold line represents the optimal convergence rate.

and from the condition in Eq. (22), the following equation should be satisfied for this deformation mode

$$\tilde{e}^m_{rs}|_{\text{bil.}} = \mathbf{x}_d \cdot \mathbf{x}_d. \tag{A.9}$$

Using Eq. (A.8) in Eq. (16), the five strain coefficients in Eq. (18) become

$$\left(e^m_{rr}|_{\text{con.}} + e^m_{rs}|_{\text{bil.}}\right) = \mathbf{x}_d \cdot \mathbf{x}_d, \quad (e^m_{ss}|_{\text{con.}} + e^m_{rs}|_{\text{bil.}}) = \mathbf{x}_d \cdot \mathbf{x}_d, \quad e^m_{rs}|_{\text{con.}} = 0,$$
$$e^m_{rr}|_{\text{lin.}} = \mathbf{x}_r \cdot \mathbf{x}_d, \quad e^m_{ss}|_{\text{lin.}} = \mathbf{x}_s \cdot \mathbf{x}_d. \tag{A.10}$$

Substituting Eqs. (A.9) and (A.10) into Eq. (A.7), the constant d is determined

$$d = c_r^2 + c_s^2 - 1, \tag{A.11}$$

which can be rewritten as

$$d = (c_r+1)(c_r-1) + (c_s+1)(c_s-1) + 1$$
$$= [(\mathbf{x}_d + \mathbf{x}_r)\cdot\mathbf{m}^r][(\mathbf{x}_d - \mathbf{x}_r)\cdot\mathbf{m}^r] + [(\mathbf{x}_d + \mathbf{x}_s)\cdot\mathbf{m}^s][(\mathbf{x}_d - \mathbf{x}_s)\cdot\mathbf{m}^s] + 1. \tag{A.12}$$

Using Eq. (13) in Eq. (A.12), the constant d becomes

$$d = (\mathbf{x}_e^2 \cdot \mathbf{m}^s)(\mathbf{x}_e^4 \cdot \mathbf{m}^s) + (\mathbf{x}_e^3 \cdot \mathbf{m}^r)(\mathbf{x}_e^1 \cdot \mathbf{m}^r) + 1 \tag{A.13}$$

and the constants in Eq. (24) are finally obtained from Eq. (A.7).

References

[1] Ko Y, Lee PS, Bathe KJ. The MITC4+ shell element and its performance. Comput Struct 2016;169:57–68.
[2] Dvorkin EN, Bathe KJ. A continuum mechanics based four-node shell element for general nonlinear analysis. Eng Comput 1984;1(1):77–88.
[3] Bathe KJ. Finite element procedures. 2nd ed. Watertown, MA: Klaus-Jürgen Bathe; 2014.
[4] Bathe KJ. The inf–sup condition and its evaluation for mixed finite element methods. Comput Struct 2001;79(2):243–52.
[5] Bathe KJ, Iosilevich A, Chapelle D. An inf-sup test for shell finite elements. Comput Struct 2000;75(5):439–56.
[6] Chapelle D, Bathe KJ. The finite element analysis of shells – fundamentals. 2nd ed. Berlin: Springer; 2011.
[7] Chapelle D, Bathe KJ. Fundamental considerations for the finite element analysis of shell structures. Comput Struct 1998;66(1):19–36. 711–2.
[8] Lee PS, Bathe KJ. On the asymptotic behavior of shell structures and the evaluation in finite element solutions. Comput Struct 2002;80(3):235–55.

[9] Bathe KJ, Dvorkin EN. A formulation of general shell elements – the use of mixed formulation of tensorial components. Int J Numer Meth Eng 1986;22(3):697–722.
[10] Bucalem ML, Bathe KJ. Higher-order MITC general shell elements. Int J Numer Meth Eng 1993;36(21):3729–54.
[11] Bucalem ML, Bathe KJ. Finite element analysis of shell structures. Archiv Comput Meth Eng 1997;4(1):3–61.
[12] Vampa V. Analysis of in-layer strains in the low order MITC shell element. Latin Am J Solid Struct 2007;4(2):87–102.
[13] Bathe KJ, Lee PS, Hiller JF. Towards improving the MITC9 shell element. Comput Struct 2003;81(8):477–89.
[14] da Veiga LB, Chapelle D, Suarez IP. Towards improving the MITC6 triangular shell element. Comput Struct 2007;85(21):1589–610.
[15] Lee PS, Bathe KJ. Development of MITC isotropic triangular shell finite elements. Comput Struct 2004;82(11):945–62.
[16] Lee Y, Yoon K, Lee PS. Improving the MITC3 shell finite element by using the Hellinger-Reissner principle. Comput Struct 2012;110–111:93–106.
[17] Lee Y, Lee PS, Bathe KJ. The MITC3+ shell element and its performance. Comput Struct 2014;138:12–23.
[18] Kim DN, Bathe KJ. A triangular six-node shell element. Comput Struct 2009;87(23):1451–60.
[19] Lee Y, Jeon HM, Lee PS, Bathe KJ. The modal behavior of the MITC3+ triangular shell element. Comput Struct 2015;153:148–64.
[20] Zienkiewicz OC, Taylor RL, Too JM. Reduced integration technique in general analysis of plates and shells. Int J Numer Meth Eng 1971;3(2):275–90.
[21] Belytschko T, Tsay CS. A stabilization procedure for the quadrilateral plate element with one-point quadrature. Int J Numer Meth Eng 1983;19(3):405–19.
[22] Belytschko T, Leviathan I. Projection schemes for one-point quadrature shell elements. Comp Meth Appl Mech Eng 1994;115(3):277–86.
[23] Choi CK, Paik JG. An efficient four node degenerated shell element based on the assumed covariant strain. Struct Eng Mech 1994;2(1):17–34.
[24] Roh HY, Cho M. The application of geometrically exact shell elements to B-spline surfaces. Comp Meth Appl Mech Eng 2004;193(23):2261–99.
[25] Kulikov GM, Plotnikova SV. A family of ANS four-node exact geometry shell elements in general convected curvilinear coordinates. Int J Numer Meth Eng 2010;83(10):1376–406.
[26] Lee PS, Bathe KJ. Insight into finite element shell discretizations by use of the "basic shell mathematical model". Comput Struct 2005;83(1):69–90.
[27] Prathap G. A C0 continuous four-noded cylindrical shell element. Comput Struct 1985;21(5):995–9.
[28] Bathe KJ, Iosilevich A, Chapelle D. An evaluation of the MITC shell elements. Comput Struct 2000;75(1):1–30.
[29] Hiller JF, Bathe KJ. Measuring convergence of mixed finite element discretizations: an application to shell structures. Comput Struct 2003;81(8):639–54.
[30] Lee PS, Bathe KJ. The quadratic MITC plate and MITC shell elements in plate bending. Adv Eng Software 2010;41(5):712–28.
[31] Batoz JL, Bathe KJ, Ho LW. A study of three-node triangular plate bending elements. Int J Numer Meth Eng 1980;15(12):1771–812.
[32] Klinkel S, Gruttmann F, Wagner W. A robust non-linear solid shell element based on a mixed variational formulation. Comp Meth in App Mech Eng 2006;195(1):179–201.
[33] Sussman T, Bathe KJ. 3D-shell elements for structures in large strains. Comput Struct 2013;122:2–12.
[34] Jeon HM, Lee Y, Lee PS, Bathe KJ. The MITC3+ shell element in geometric nonlinear analysis. Comput Struct 2015;146:91–104.